https://doi.org/10.5194/amt-2023-180
Preprint. Discussion started: 20 November 2023

Atmospheric Measurement Techniques Discussions

Martian column CO_2 and pressure measurement with differential absorption lidar at 1.96 μm

Zhaoyan Liu[1], Bing Lin[1], Joel Campbell[1], Jirong Yu[2], Jihong Geng[3], and Shibin Jiang[3]

[1]NASA Langley Research Center, Hampton, VA23681, USA
[2]Science Technology Corporation, Hampton, VA23666, USA
[3]AdValue Photonics, Inc, Tucson, AZ85714, USA

Correspondence to: Zhaoyan Liu (Zhaoyan.liu@nasa.gov)

Abstract. By utilizing progress in millijoule-level pulsed fiber lasers operating in the 1.96 μm spectral range, we introduce a concept utilizing a differential absorption barometric lidar designed to operate within the 1.96 μm CO_2 absorption band for remote sensing of Martian atmospheric properties. Our focus is on the online wavelength situated in the trough region of two absorption lines, selected due to its insensitivity to laser frequency variations, thus mitigating the necessity for stringent laser frequency stability. Our investigation revolves around a compact lidar configuration, featuring reduced telescope dimensions and lower laser pulse energies. These adjustments are geared towards minimizing costs for potential forthcoming Mars missions. The core measurement objectives encompass the determination of column CO_2 absorption optical depth, columnar CO_2 abundance, surface air pressure, as well as vertical distributions of dust and cloud layers. Through the amalgamation of surface pressure data with atmospheric temperature insights garnered from sounders and utilizing the barometric formula, the prospect of deducing atmospheric pressure profiles becomes feasible. Simulation studies validate the viability of our approach. Notably, the precision of Martian surface pressure measurements is projected to surpass 1 Pa when the aerial dust optical depth is projected to be under 0.7, a typical air borne dust scenario on Mars, considering a horizontal averaging span of 10 km.

1 Introduction

Atmospheric temperature and pressure play pivotal roles in determining the states and dynamics of extraterrestrial planetary atmospheres within the solar system. The temperature structure of the atmosphere is governed by thermodynamics and dynamics, particularly the heating from solar radiation and thermal emission from the surface and atmosphere. Meanwhile, pressure and pressure gradients serve as the primary driving forces for atmospheric motion and the transport of mass, heat, and momentum (Holton, 1979). Dry air movements on extraterrestrial planets represent crucial atmospheric dynamic processes, heavily influenced by radiative heating and pressure fields. In the case of the Martian atmosphere, these dynamic processes can produce synoptic scale storm systems characterized by significant winds and dusts activity. Accurate observation, modeling, and prediction of temperature, pressure, and dust aerosol fields on Mars are vital for understanding Martian weather systems, particularly the occurrence of dust storms. Moreover, these efforts provide invaluable support for safe and accurate atmospheric entry, suitable landing site selection, and ultimately human colonization of Mars.

The Martian atmosphere is predominantly composed of carbon dioxide (approximately 95.32%), along with small amounts of nitrogen and argon (approximately 2.6% and 1.9%, respectively). It also contains traces of oxygen, water vapor, carbon monoxide, hydrogen, and other noble gases (Franz et al., 2017; Williams, 2020). Understanding the global atmospheric dynamics, thermodynamics, dust storms, and variations in the carbon cycle on Mars is crucial for successful Mars exploration. Remote sensing techniques may be the only practical means to observe and gain knowledge about these processes and variations.

Planetary atmospheric temperature can be measured globally by infrared (IR) remote sensing techniques. However, air pressure measurements, even on Earth, are very limited. Currently, only extremely sparse in-situ measurements from buoys, ships, or dropsondes are available over open oceans in Earth's atmosphere. Global operational measurements of pressure fields are not yet available, as reviewed in Lin and Hu (2005) and Lawrence et al. (2011).

For the Martian atmosphere, surface air pressure measurements have been conducted at specific locations using in-situ barometers on missions such as Viking Landers, Mars Pathfinder, Phoenix Mars Lander, Mars Science Laboratory, and the recent InSight mission (Banfield et al., 2020).

Passive instruments like the near-infrared imaging spectrometer (Forget et al., 2007; Spiga et al., 2007), Mars Express OMEGA visible and near-infrared imaging spectrometer (Forget et al., 2007; Spiga et al., 2007), and the IMS (Imaging Spectrometer) that was Phobos2 (Bibring et al., 1991) made it possible to do large-scale surface pressure mapping on Mars and have been used to measure the amount of CO_2 in the 2-µm CO_2 absorption band using reflected solar radiation..

While surface pressure observations obtained through passive remote sensing techniques offer valuable insights into the dynamics of the Martian atmosphere, they have certain limitations. Critical issues of these techniques include: (1) Air pressure measurements using the passive technique can only be performed during daytime, restricting the temporal coverage of observations. (2) The absence of ranging capability in passive measurements may introduce systematic errors. Dust and cloud reflections can result in different path lengths of sunlight compared to surface reflections, leading to uncertainties in the derived pressure values. (3) Observations of CO_2 changes and pressure fields are unavailable in certain crucial regions, such as the two polar regions. This limitation hinders our understanding of the Martian carbon cycle, dynamics, and the interaction between polar regions and lower latitudes. (4) Passive measurements are confined to surface pressure fields and cannot account for sufficient information regarding surface elevation variations. The Martian atmosphere is characterized by ubiquitous airborne dust, which can interfere with passive measurements. Additionally, the terrain surface on Mars exhibits significant changes at various spatial scales (Frey et al., 1998; Smith et al., 1999), potentially introducing bias into passive measurements.

Our previous study (Lin and Liu, 2021) proposed the integration of active sensors into the existing suite of pressure sensing instruments for Martian atmospheric studies and Mars exploration. Specifically, a pulsed CO_2 differential absorption lidar (DIAL) operating at the 2.05-µm CO_2 absorption band was simulated and evaluated. Unlike passive sensors that are limited to

https://doi.org/10.5194/amt-2023-180
Preprint. Discussion started: 20 November 2023

Atmospheric Measurement Techniques Discussions

column CO_2 measurements, which can be biased by the presence of clouds and/or dust aerosols, a pulsed DIAL system enables the collection of range-resolved return signals from all atmospheric backscattering targets, including aerosols, clouds, and the surface. Consequently, when combined with an infrared temperature sounder, the DIAL system has the potential to provide vertical profile measurements of pressure (Lin and Liu, 2021). Furthermore, a DIAL system offers advantages such as suitability for pressure measurements over varying topography, the ability to operate during both day and night, and the capability to obtain measurements over polar regions.

This study reexamines the concept of Martian pressure measurement and explores additional opportunities within the 1.96 µm CO_2 absorption band. Recent advancements in all-fiber lasers have demonstrated the generation of millijoule-level pulses with kilohertz repetition frequencies, enabling high transmitted powers at this wavelength band. Considering the size, weight, and power (SWaP) constraints crucial for space-based systems, particularly for Mars mission lidars, this study utilizes a compact telescope and focuses on the column CO_2 and pressure measurement. Furthermore, the online wavelength is selected at the trough region between two adjacent absorption lines. This choice can reduce the sensitivity to laser frequency variability (Korb and Weng, 1983) and thereby relax the stringent requirements for laser frequency stability.

2. Methodology of the DIAL System

2.1 DIAL Measurement

In the CO_2 differential absorption measurement, it is common practice to choose two or more wavelengths (Abshire et al., 2010; Lin et al., 2013; Refaat et al., 2015). One wavelength, referred to as the offline wavelength, is selected far from the center of the absorption line where the CO_2 absorption is insignificant, serving as a baseline reference. The other wavelengths, known as the online wavelengths, are chosen on the line where the CO_2 absorption is substantial, enabling accurate measurement of CO_2 concentrations. The selected online and offline wavelengths are closely positioned, resulting in negligible differences in scattering optical depths between these wavelengths. The CO_2 differential absorption optical depth (DAOD) can then be determined by calculating the ratio of received signals at the online and offline wavelengths (Lin and Liu, 2021):

$$\Delta\tau_{CO_2} = -\frac{1}{2}\ln\left(\frac{S_{on}}{S_{off}}\frac{C_{off}}{C_{on}}\right). \tag{1}$$

$\Delta\tau_{CO2}$ represents the CO_2 DAOD at the online and offline wavelengths. S_{on} and S_{off} correspond to the received signals at the online and offline wavelengths, respectively. C_{on} and C_{off} denote the calibration coefficients for the online and offline wavelengths, respectively. In practical applications, the ratio of C_{off} to C_{on} is required to derive $\Delta\tau_{CO2}$. This ratio can be obtained through the zero-range measurements where the CO_2 absorption is effectively zero (Lin et al., 2015; Dobler et al., 2013; Campbell et al., 2020). The CO_2 DAOD can be expressed as:

$$\Delta\tau_{CO_2} = \int_z^{TOA}\left[\alpha_{CO_2,on}(z') - \alpha_{CO_2,off}(z')\right] n_{CO_2}(z')\,dz' = \mathrm{A}_{CO_2}(z)\,N_{CO_2}(z), \tag{2}$$

https://doi.org/10.5194/amt-2023-180
Preprint. Discussion started: 20 November 2023

Atmospheric Measurement Techniques
Discussions

where $\alpha_{CO2}(z)$ and $n_{CO2}(z)$ are the CO_2 absorption cross section and number density at altitude *z*, respectively. $N_{CO2}(z)$ is the column CO_2 molecular number integrated from *z* to the top of atmosphere (TOA). $A_{CO2}(z)$ is a mean differential absorption cross section from *z* to TOA weighted by CO_2 number density,

$$A_{CO_2}(z)=\frac{\int_z^{TOA}\left[\alpha_{CO_2,on}(z')-\alpha_{CO_2,off}(z')\right]n_{CO_2}(z')dz'}{\int_z^{TOA}n_{CO_2}(z')dz'}. \tag{3}$$

From Eq. (2), we derive:

$$N_{CO_2}(z)=\frac{\Delta\tau_{CO_2}(z)}{A_{CO_2}(z)}, \tag{4}$$

and this molecular number determines the air pressure caused by CO_2:

$$P_{CO_2}(z)=M_{CO_2}g_W(z)N_{CO_2}(z), \tag{5}$$

where M_{C02} is the CO_2 molecular mass, and

$$g_W(z)=\frac{\int_z^{TOA}g(z')n_{CO_2,\mathrm{model}}(z')dz'}{\int_z^{TOA}n_{CO_2,\mathrm{model}}(z')dz'} \tag{6}$$

is a weighted mean Martian gravitational acceleration between *z* and TOA, *g(z)* the gravitational acceleration at altitude *z*. The Martian atmospheric pressure is the sum of CO_2 pressure and the pressure of all other gases $P_{\mathrm{other}}(z)$

$$P(z)=P_{CO_2}(z)+P_{others}(z). \tag{7}$$

The Martian atmosphere is predominantly composed of carbon dioxide. The pressure exerted by other gases on Mars, P_{others}, is small and remains relatively stable. The determination of P_{others} can be achieved through climatological analysis or other dedicated measurements.

2.2 Surface Column CO_2 and Pressure Measurement

In our previous study (Lin and Liu, 2021), we proposed a DIAL system with a telescope size of 1 m and a laser pulse energy of 5 mJ at the online wavelengths. The system was designed for atmospheric profiling and column measurements of CO_2 and pressure. However, in this current study, our focus is on the measurement of the crucial dynamic variable, surface air pressure. Consequently, we can reduce the telescope size and laser pulse energy to build a more compact lidar system. As illustrated by the simulation results presented in Section 3.2, the reduction in telescope size and pulse energy presents challenges for accurately measuring atmospheric CO_2 DAOD. However, the surface return signal remains sufficiently strong to enable precise measurement of CO_2 DAOD, from which surface pressure can be accurately derived. The surface return signal is consistently available when the airborne dust load is low or moderate.

https://doi.org/10.5194/amt-2023-180
Preprint. Discussion started: 20 November 2023

Atmospheric Measurement Techniques Discussions

2.3 Atmospheric Pressure Measurement with IR Sounder Temperature Measurement

While the DIAL system considered in this study may not allow for atmospheric vertical profiling of CO_2 DAOD due to weaker lidar return signals compared to our previous study (Lin and Liu, 2021, and Section 3), it is still possible to derive vertical profiles of atmospheric pressure. This can be accomplished by leveraging surface pressure measurements and infrared (IR) temperature profile measurements. IR sounders are compact and cost-effective sensors commonly used for satellite temperature measurements (Kalmus et al., 2022; Natraj et al., 2022).

Given the temperature T(z) measured by the sounder at a specific altitude z, the pressure can be determined using the barometric formula:

$$P(z) = P_0 e^{-\int_0^z \frac{M_{Mars} g(z)}{RT(z)} dz}. \tag{8}$$

Where P_0 represents a reference pressure at the surface or an altitude where a CO_2 DAOD is available from a dense dust layer or cloud, M_{Mars} = 0.04334 kg/mole denotes the molar mass of Martian air, and R = 8.314 $\mathrm{JK^{-1}mol^{-1}}$ represents the universal gas constant.

To calculate P(z) using Eq. (8), the reference pressure P_0 is required. P_0 can be obtained from the DIAL CO_2 DAOD measurement at the surface. However, to accurately calculate the weighting function A_{CO2} in Eq. (3) and, subsequently, P_{CO2} in Eq. (5), some knowledge about the temperature and pressure profiles is necessary. Hence, an iterative procedure is applied. Initially, a climatological or modeled value P_{0c} can be used as an estimate for the surface pressure to calculate the first set of P(z) using Eq. (8). With the initially calculated P(z) and the temperature profile T(z) obtained from the sounder measurements, the weighting function A_{CO2}(z) in Eq. (3) and, consequently, the CO_2 pressure at the surface $P_{0,CO2}$ can be retrieved more accurately from the CO_2 DAOD measurement using Eq. (5). As previously mentioned, CO_2 comprises the dominant composition of the Martian atmosphere, and the pressure of other gases (P_{others}) remains relatively stable. Using $P_{0,CO2}$, the surface pressure P_0 can then be determined from $P_{0,CO2}$ using Eq. (7). Once P_0 is determined from the CO_2 DAOD measurement, it can replace the climatological or modeled value $P_{0,c}$ to recalculate P(z) using Eq. (8). This process can be repeated iteratively to improve the retrieval of P_0. In cases where very dense dust or cloud layers are present, the surface return may not be available. However, accurate CO_2 DAOD measurements may be derived from the lidar return signals from these targets. The pressure P at altitude z_0, where the dense dust or cloud layers are located, can be used as the reference P_0 in Eq. (8). The afore mentioned iterative procedure can then be applied to derive the pressure P at z_0, above and below.

2.4 Wavelength Selection

The wavelengths selected in the 2.05 µm absorption band, specifically line R(32) of the ν'(20013) vibrational band with the line center at 2.050428 µm, in our previous study (Lin and Liu, 2021) are very close to those (line R(30) of the same vibrational band) used in NASA Langley Research Center's (LaRC's) pulsed DIAL systems for CO_2 measurement on Earth (Refaat et al., 2015; Yu et al., 2017). However, the differences in line selection reflect the distinct atmospheric environments of Earth and

Mars. Compared to Earth's atmosphere with a carbon dioxide (CO_2) volume mixing ratio of approximately 400 parts per million (ppm), the Martian atmosphere is predominantly composed of CO_2, accounting for about 95.3% by volume, despite having a much lower total amount or air pressure. As a result, pressure-induced absorption line broadening is significantly smaller in the Martian atmosphere, and the line shape is much narrower. Consequently, the lidar wavelengths are typically chosen on the wing of an absorption line where the column CO_2 DAOD falls within the range of 0.5-2, with an optimal DAOD value of 1.11 (Lin and Liu, 2021).

The criteria for wavelength selection in this study are as follows: (1) the presence of a strong absorption line with a nearby weak absorption line on the wing of the strong line, (2) both the strong and weak lines are from the principal isotope $^{12}C^{16}O_2$, and (3) AOD of the trough region is approximately 1.1. While weak absorption lines from CO_2 isotopes other than $^{12}C^{16}O_2$ could also be considered, the accuracy of current knowledge regarding the abundance of these isotopes on Mars may impact spectroscopic analysis. In this study, the strong absorption line is P(10) from the $^{12}C^{16}O_2$ vibration band (ν' = 20011, with a center wavelength of 1.9640146 μm), as indicated by the red arrow in Fig. 1. The CO_2 absorption is calculated using a typical Martian atmosphere obtained from Viking 1 observations (Seiff and Kirk, 1977), as illustrated in Fig. 2. The online wavelength is set at the trough region near 1.9639572 μm of the selected strong line, along with a weak line centered at 1.9639502 μm from another $^{12}C^{16}O_2$ vibration band, as shown in Fig. 3. The modeling of the Martian atmosphere in Fig. 3 is based on the Viking 1 observation depicted in Fig. 2. The AOD is calculated using the line-by-line calculation method through the HITRAN Application Programming Interface (HAPI) (Kochanov et al., 2016). Figure 3(b) illustrates that the sensitivity of AOD to laser frequency variability is significantly smaller in the trough regions compared to the surrounding regions. Thus, in this study, the online wavelength is set in the trough region of the two selected lines. The column CO_2 AOD at the trough is approximately 0.885, corresponding to a DAOD of 0.825, which is close to the optimal value of 1.11. The change in online AOD is smaller than 10^{-4} for a 1 MHz change in laser frequency at the selected trough region, and the change in offline AOD is even smaller. These small AOD changes due to laser frequency variations lead to insignificant errors in DAOD calculations and retrievals. Consequently, the requirements for laser frequency stability can be relaxed.

It is worth noting that P(12) of the same 12C16O2 ν'(20011) vibration band could also be considered a good candidate, as it has a few weak absorption lines on its wing. However, in this study, our analysis focuses solely on P(10).

2.5 Laser and Wavelength Locking

The NASA LaRC has made significant advancements in laser frequency control and locking techniques over the past decades. Figure 4 illustrates a conceptual diagram depicting the master laser wavelength locking and control system. For this system, two or more continuous-wave single-frequency fiber or semiconductor-distributed feedback lasers can be utilized as master lasers. In this setup, one master laser is locked at the center of the selected line at 1.9640146 μm. The Pound-Drever-Hall frequency stabilization scheme is employed with a CO_2 absorption cell to achieve this locking. The other master laser, or possibly two master lasers, can be locked off the line center by 4.44 GHz for the online wavelength or -25.75 GHz for the offline wavelength. The seed lasers employed in the LaRC airborne CO_2 DIAL system can be wavelength-locked at the line center or locked up to 35 GHz from the line center, with a long-term frequency jittering of 0.3 MHz (Refaat et al., 2015; Koch et al., 2008). With the laser frequency stability achieved at this level and the online laser wavelength in the trough region, the error in DAOD due to laser frequency variability is smaller than 10^{-4}, making it insignificant for DIAL DAOD measurements. The laser transmitter considered in this study is an all-fiber master oscillator power amplifier (MOPA) system. Optical fiber amplifier technology has advanced considerably. Specifically, pulsed laser energy exceeding 1 mJ at kilohertz repetition frequencies has been demonstrated in the 1.97 µm band. These technological breakthroughs enable the development of compact and lightweight laser sources for future Mars missions.

3 Simulation

3.1 Error Analysis

Based on the first order error propagation theory, the error ε and the relative error due to random noise for all individual quantities in Eqs. (3) – (5) can be estimated (Lin and Liu, 2021) using:

$$\varepsilon_{\Delta\tau_{CO_2}(z)} = \frac{1}{2}\left(\left(\frac{1}{SNR_{on}(z)}\right)^2 + \left(\frac{1}{SNR_{off}(z)}\right)^2\right)^{1/2}, \tag{9a}$$

$$\frac{\varepsilon_{\Delta\tau_{CO_2}(z)}}{\Delta\tau_{CO_2}(z)} = \frac{1}{2\Delta\tau_{CO_2}(z)}\left(\left(\frac{1}{SNR_{on}(z)}\right)^2 + \left(\frac{1}{SNR_{off}(z)}\right)^2\right)^{1/2}, \tag{9b}$$

$$\varepsilon_{N_{CO_2}(z)} = \sqrt{\left(\frac{\sigma_{\Delta\tau_{CO_2}(z)}}{A_{CO_2}(z)}\right)^2 + \left(N_{CO_2}(z)\frac{\sigma_{A_{CO_2}(z)}}{A_{CO_2}(z)}\right)^2}, \tag{10a}$$

$$\frac{\varepsilon_{N_{CO_2}(z)}}{N_{CO_2}(z)} = \sqrt{\left(\frac{\varepsilon_{\Delta\tau_{CO_2}(z)}}{\Delta\tau_{CO_2}(z)}\right)^2 + \left(\frac{\varepsilon_{A_{CO_2}(z)}}{A_{CO_2}(z)}\right)^2}, \tag{10b}$$

$$\varepsilon_{P_{CO_2}(z)} = M_{CO_2} g_W(z)\, \varepsilon_{N_{CO_2}(z)}, \tag{11a}$$

$$\frac{\varepsilon_{P_{CO_2}(z)}}{P_{CO_2}(z)} = \frac{\varepsilon_{N_{CO_2}(z)}}{N_{CO_2}(z)} = \frac{\varepsilon_{\Delta\tau_{CO_2}(z)}}{\Delta\tau_{CO_2}(z)}. \tag{11b}$$

These results demonstrate that the relative errors in the measured CO_2 DAOD are equivalent to the corresponding relative errors in the observations of CO_2 amount and air pressure. As discussed in Section 2.3, the vertical profile of atmospheric pressure can be derived using Eq. (8) when the atmospheric temperature profile is measured using an IR sounder. The error and relative error in the retrieval of atmospheric pressure can be estimated using the following equations:

$$\varepsilon_{P(z)} = \sqrt{\left(e^{-\int_0^z \frac{M_{Mars} g(z)}{RT(z)} dz} \cdot \varepsilon_{P_0}\right)^2 + \left(P_0 e^{-\int_0^z \frac{M_{Mars} g(z)}{RT(z)} dz} \int_0^z \frac{M_{Mars} g(z)}{RT^2(z)} dz \cdot \varepsilon_{T(z)}\right)^2} \tag{12a}$$

$$\frac{\varepsilon_{P(z)}}{P(z)} = \sqrt{\left(\frac{\varepsilon_{P_0}(z)}{P_0}\right)^2 + \left(\int_0^z \frac{M_{Mars} g(z)}{RT(z)} \frac{\varepsilon_{T(z)}}{T(z)} dz\right)^2} . \tag{12b}$$

205 The first term in Eq. (12a) and (12b) represents the contribution of the error in the surface pressure P_0, which is used to calculate the atmospheric pressure P using Equation (8). This term includes the error in the retrieved $P_{0,CO2}$ from the CO_2 DAOD measurement and the error in the pressure of other gases (P_{others}). While it is challenging to estimate the exact error in P_{others}, it is anticipated to be small. This is because P_{others} is relatively stable and constitutes only a small fraction of the total Martian atmospheric pressure (< 5%).

210 Random errors in the measured temperature T can be partially smoothed out through the integration calculation in Eq. 8. However, it's important to note that any systematic error in T cannot be reduced by integration or signal averaging, and such systematic errors can propagate into the retrieval of atmospheric pressure P using Eq. 8. A study by Natraj et al. (2022) demonstrated that the total error in temperature measurements for the JPL GEO-IR Sounder ranges from 0.3-1 K, with a precision of 0.1-0.3 K. Data fusion techniques that combine measurements from multiple satellite sounders have been shown

215 to reduce bias in near-surface temperature measurements, resulting in mean biases smaller than 0.16 K (Kalmus et al., 2022). Considering these low bias errors, this study conservatively assumes potential temperature bias errors within 2 K.

The error and relative error in atmospheric pressure P (i.e., the second term in Eq. (12a) and (12b)) can be estimated as a function of altitude, considering different biases in temperature T of ±0.5 K, ±1.0 K, and ±2.0 K. These estimations are presented in Fig. 5. From Fig. 5, it can be observed that the bias in temperature T has a minimal impact on the retrieval of

220 atmospheric pressure near the surface. However, as altitude increases, the influence of the temperature bias on pressure retrieval becomes relatively more significant (Fig. 5a). This is due to the cumulative effect of the temperature bias as altitude increases (via the integration term in Eq. 12). The absolute error in atmospheric pressure P (as shown in Fig. 5b) due to the temperature bias is very small near the surface. It gradually increases with altitude, reaching a maximum around 12 km, and then decreases. This trend is primarily driven by the decreasing trend of air pressure with increasing altitude.

225 Systematic errors or biases in temperature can further propagate to the retrieval of CO_2 pressure (P_{CO2}) using Eq. (5) through the calculation of the weighting function (A_{CO2}). To assess the impact of T biases on P_{CO2}, errors and relative errors in P_{CO2} as a function of altitude are simulated using the HAPI software for T biases of ±0.5 K, ±1.0 K, and ±2.0 K. The results are presented in Fig. 6. In Fig. 6, the curves represent the systematic errors or relative systematic errors in P_{CO2} at different altitudes resulting from the T bias. The magnitudes of the relative errors initially decrease with increasing altitude until approximately

1.4 km, after which they start to increase. At z = 0 (representing the surface in this study), the magnitudes of the relative errors in P_{CO2} are smaller than 0.1% (Fig. 6a), and the absolute errors are smaller than 0.5 Pa (Fig. 6b) when the T bias is smaller than 2 K. The magnitudes of errors reach a maximum around 14 km, remaining below 1.6 Pa when the T bias is smaller than 2 K.

3.2 Simulation Results

When comparing the CO_2 DIAL measurement on Mars to the CALIPSO lidar measurement on Earth (Hunt et al., 2009), several advantages of space lidar measurements on Mars can be observed. These advantages are summarized in Table 1. On Mars, the smaller size and mass of the planet, as well as the greater distance from the Sun, contribute to the advantages of space lidar measurements. A lower orbit height on Mars results in a figure of merit (FOM) of 8.05, as the received signal is proportional to the squared range from the lidar to the atmospheric backscatter. Slower ground speed on Mars allows for a longer averaging time for a given horizontal distance, leading to a FOM of 2.17. Moreover, the photon number per unit pulse energy is 3.9 times larger at 1.964 µm compared to the visible region at 0.532 µm. The combined effect of these factors yields a FOM of approximately 67, which is a significant advantage. This allows for the use of lower laser power and/or smaller receiving telescope size, resulting in a more compact lidar system. Furthermore, the solar radiation constant on Mars is 2.3 times smaller than on Earth, and the solar radiation at 1.964 µm is approximately 220 times smaller than in the visible region. As a result, the daytime background noise, which is the dominant noise source in visible lidar measurements on Earth, is significantly reduced in the Mars measurement. This reduction in noise further enhances the performance of the DIAL system. Considering these advantages, a compact DIAL system for Mars can be developed with relatively small telescope size and laser pulse energy. The specific parameters are listed in Table 2, and they can be achieved using currently available technologies, parts, and devices.

To assess the impact of detection noises and evaluate the performance of the DIAL system, observing system simulation experiments (OSSEs) are conducted. These OSSEs are based on the system parameters listed in Table 2. It should be noted that these parameters are similar to those used in Lin and Liu (2021), with a few differences. In this study, the telescope size is reduced to 0.3 meters, which is approximately 3.3 times smaller than in the previous study. Additionally, the laser output energy for both the online and offline wavelengths is set to 1.5 mJ, whereas the previous study assumed values of 5 mJ for the online wavelength and 2 mJ for the offline wavelength. It is worth mentioning that recent advancements in all-fiber MOPA lasers have demonstrated laser output energies close to 2 mJ at the selected wavelengths, supporting the feasibility of the system parameters proposed in this study.

The OSSEs specifically focus on random errors caused by detection noises. The experiments provide valuable insights into the system's sensitivity, accuracy, and overall performance, thereby guiding further improvements and developments in the field of DIAL technology for Mars exploration.

For the detector in the DIAL system, a HgCdTe Avalanche Photodiode (APD) is assumed, which is currently used for spaceborne lidar applications in the IR region (Lin et al., 2013; Sun et al., 2017). The selection of this detector is based on its

https://doi.org/10.5194/amt-2023-180
Preprint. Discussion started: 20 November 2023

suitability for the desired performance and requirements of the lidar system. Furthermore, the optical parameters of the lidar system, including the field of view (FOV), beam expander, and transceiver throughputs, are adapted from the CALIPSO backscatter lidar. CALIPSO is a backscatter lidar that was launched in 2006 (Hunt et al., 2009) and has been nearly continuously operating in space. By utilizing these established optical parameters, the DIAL system can benefit from the experience and success of the CALIPSO mission. These optical parameters, along with the choice of a suitable detector, contribute to the overall design and performance of the DIAL system, enabling accurate and reliable measurements of atmospheric parameters for Mars exploration.

Fig. 7. shows the OSSE results, where Figure 7a shows the modeled dust profile based on the SPICAM's dust vertical distribution occultation measurement on Mars-Express (Fedorova et al., 2009). The dust distribution was extrapolated to the surface using an exponential curve and the occultation measurement was conducted above 10 km. The modeled dust column optical depth from TOA to the surface is 0.373 at 1.964 µm. In the presence of the modeled dust, the online signal-to-noise ratio (SNR) is too small in the atmosphere to accurately profile CO_2 DAOD and pressure, as shown in Fig. 7b. However, during nighttime, the offline SNR is greater than 10 below ~14 km with a horizontal resolution of 10 km and vertical resolution of 1 km. With further averaging, if needed, these measurements can provide dust profiles in the lower atmosphere.

For the daytime simulation, the online and offline SNRs experience a decrease due to the presence of solar background noise. However, the decrease is not significant compared to the nighttime SNRs. This is because the solar background radiation at 1.964 µm is significantly smaller compared to the CALIPSO aerosol measurement at 532 nm (Hunt et al., 2009). It is important to note that the worst-case scenario of a Sun zenith angle (SZA) of 30°, corresponding to the SZA at the equator where the background noise is the strongest, is considered in the daytime simulation. This indicates that the DIAL system can maintain reasonable SNRs even in the presence of solar background noise during daytime operations. These OSSE results provide valuable insights into the performance and limitations of the DIAL system in the presence of dust and under different lighting conditions.

Dust on Mars exhibits significant annual and geophysical variations, leading to fluctuations in dust optical depth (OD) ranging from approximately 0.4 to 1.4 at 880 nm (Chen-Chen et al., 2019). During the 34 global dust storm on Mars, the dust OD was as high as approximately 8 (Guzewich et al., 2019). In cases of heavy dust loading, the DIAL system considered in this study may enable measurements of CO_2 DAOD and pressure in the Martian atmosphere. While the SNR in the atmosphere is generally too low to achieve accurate measurements of Martian CO_2 DAOD and pressure, the lidar return signal from the surface is several orders of magnitude stronger. This allows for precise retrieval of column CO_2 DAOD and surface air pressure from the lidar surface return. Figure 7c and 7d illustrate the relative error and error, respectively, in surface CO_2 DAOD ($\Delta\tau_{CO2}$) and pressure P_{CO2} simulated for both nighttime and daytime scenarios at a horizontal resolution of 10 km.

Interestingly, the curves for nighttime and daytime measurements closely overlap due to the strong surface return signal, which results in signal shot noise dominating the measurement when a commercial solar blocking filter of 0.8 nm is utilized. The relative error in CO_2 DAOD remains below 0.2% when the dust OD is approximately 1 or lower. Similarly, the error in $P_{0,CO2}$

https://doi.org/10.5194/amt-2023-180
Preprint. Discussion started: 20 November 2023

Atmospheric Measurement Techniques Discussions

stays below 1 Pa when the dust OD is around 0.7 or lower. As the dust OD increases, the error in both measurements rises, but remains below 1.6 Pa until the dust OD reaches 1.

4 Conclusions

In our previous study, we proposed a novel concept utilizing a differential absorption barometric lidar operating at the 2.05 µm CO_2 absorption band (ν′ = 20013) for remote sensing of Martian atmospheric CO_2 amount and air pressure (Lin and Liu, 2021). The present study expanses the selection of laser wavelengths to the 1.96 µm CO_2 absorption band (ν′ = 20011) to leverage the recent advancements in millijoule-level pulsed fiber lasers at this wavelength. Furthermore, the online wavelength is set at the trough region of two absorption lines, where the CO_2 AOD exhibits insensitivity to the laser frequency variability. This characteristic significantly relaxes the requirement for laser frequency stability. Our measurements will focus on column CO_2 differential aerosol optical depth (DAOD), column CO2 amount, and surface air pressure using a compact telescope with a size of 0.3 m and a laser pulse energy of 1.5 mJ at a repetition frequency of 2 kHz. With this considered differential absorption lidar (DIAL) system, we can retrieve CO_2 pressure at the surface or in the atmosphere where dense dust/cloud layers are present during both day and night. Additionally, the atmospheric pressure profiles can be derived by combining the DIAL surface pressure measurements with atmospheric temperature observations obtained from sounders based on the barometric formula. Furthermore, the observation of dust and cloud vertical distributions at low altitudes is possible.

OSSE simulations were performed to estimate noise-induced random error. The results indicate that a relative error smaller than 0.2% is achievable for surface CO_2 DAOD and pressure P_{CO2} measurements at a horizontal average of 10 km when the airborne dust OD is small than 1, a condition in which the Martian airborne dust is commonly observed. An error for P_{CO2} smaller than 1 Pa is possible at the surface when the dust OD is smaller than 0.7. Achieving such measurement precision would facilitate the collection of crucial data for Mars's climate studies, enabling the acquisition of dynamic information to enhance forecasts of Martian weather and climate systems. Furthermore, future efforts in instrumentation development and exploration of atmospheric CO_2 measurements would expand the application to Martian atmospheric entry, landing site selection, severe dust storm prediction, and ultimately future human missions.

Acknowledgements

Authors are grateful for Dr Robert Hargreaves at the Center for Astrophysics, Harvard & Smithsonian for the helpful discussion on calculating the Martian CO2 spectroscopic characteristics using the HAPI software. This study is supported by the NASA’s Planetary Instrument Concepts for the Advancement of Solar System Observations (PICASSO) Program.

References

Abshire, J. B., Riris, H., Allan, G. R., Weaver, C. J., Mao, J., Sun, X., Hasselbrack, W. E., Kawa, S. R., and Biraud, S.: Pulsed airborne lidar measurements of atmospheric CO2 column absorption. Tellus B, 62, 770–783, 2010.

Banfield, D., et al.: InSight Auxiliary Payload Sensor Suite (APSS), Space Sci Rev , 215:4, https://doi.org/10.1007/s11214-018-0570-x, 2019.

Banfield, D., et al.: The atmosphere of Mars as observed by InSight. Nature Geoscience, 13, 190–198. https://doi.org/10.1038/s41561-020-0534-0, 2020.

Bibring, J.-P., Erard, S., Gondet, B., and coauthors: Topography of the martian tropical regions with ISM, Planetary and Space Science, 225-236, 1991.

Campbell, J., Lin, B., Browell, E., Obland, M., Dobler, J., Erxleben, W., McGregor, D., O'Dell, C., Bell, E., Pal, S., Weir, B., Fan, T., Kooi, S., Corbett, A., Davis, K., Gordon, I., Kochanov, R.: Field Evaluation of Column CO_2 Retrievals from Intensity-Modulated Continuous-Wave Differential Absorption Lidar Measurements during ACT-America, Earth and Space Science (DOI: 10.1029/2019EA000847), 2020.

Chen-Chen, H., Pérez-Hoyos ,S., and Sánchez-Lavega, A.: Dust particle size and optical depth on Mars retrieved by the MSL navigation cameras, Icarus, 319, 43-57, 2019.

Dobler, J. T., Harrison, F. W., Browell, E. V., Lin, B., McGregor, D., Kooi, S., Choi, Y., and Ismail, S.: Atmospheric CO2 column measurements with an airborne intensity-modulated continuous wave 1.57 µm fiber laser lidar, Applied Optics, 52 (12), 2874-2892, 2013.

Fedorova, A., Korableva, O., Bertauxb, J.-L., Rodina, A.V., Montmessin, F., Belyaeva, D. A., Reberac, A.: Solar infrared occultation observations by SPICAM experiment on Mars-Express: Simultaneous measurements of the vertical distributions of H2O, CO2 and aerosol, Icarus, 200, 96–117, 2009.

Forget, F., A. Spiga, B. Dolla, S. Vinatier, R. Melchiorri, P. Drossart, A. Gendrin, J.-P. Bibring, Y. Langevin, and B. Gondet: Remote sensing of surface pressure on Mars with the Mars Express/OMEGA spectrometer: 1. Retrieval method, J. Geophys. Res., doi:10.1029/2006JE002871, 2007.

Franz, H.; Trainer, M., Malespin, C., Mahaffy, P., Atreya, S., Becker, R., Benna, M., Conrad, P., Eigenbrode, J.: Initial SAM calibration gas experiments on Mars: Quadrupole mass spectrometer results and implications, Planetary and Space Science, 138, 44–54, Bibcode:2017P&SS44F. doi:10.1016/j.pss.2017.01.014. ISSN 0032-0633, 2017.

Frey, H., Sakimoto, S., Roark, J.: The MOLA topographic signature at the crustal dichotomy boundary zone on Mars, Geophysical Research Letters, 25, 4409-4412, 1998.

Guzewich, S. D., Lemmon, M., Smith, C. L., Martínez, G., de Vicente-Retortillo, Á., Newman, C. E., et al.: Mars Science Laboratory observations of the 2018/Mars year 34 global dust storm, Geophysical Research Letters, 46, 71–79. https://doi.org/10.1029/2018GL080839, 2019.

Holton, J., An Introduction to Dynamic Meteorology. 3rd edition, Academic Press.

https://doi.org/10.5194/amt-2023-180
Preprint. Discussion started: 20 November 2023

Atmospheric Measurement Techniques Discussions

Hunt, W., Winker, D., Vaughan, M., Powell, K., Lucker, P., and Weimer, C.: CALIPSO lidar description and performance assessment, J. Atmos. Oceanic Technol., 26, 1214–1228, 2009.

Kalmus, P., Nguyen, H., Roman, J., Wang, T., Yue, Q., Wen, Y., et al.: Data fusion of AIRS and CrIMSS near surface air temperature, Earth and Space Science, 9, e2022EA002282. https://doi. org/10.1029/2022EA002282, 2022.

Koch, G., Beyon, J., Gibert, F., Barnes, B., Ismail, S., Petros, M., Petzar, P., Yu, J., Modlin, E., Davis, K., and Singh, U.: Side-line tunable laser transmitter for differential absorption lidar measurement of CO2: design and application to atmospheric measurements, Appl. Opt. 47, 944–956, 2008.

Kochanov R. V., Gordon, I. E., Rothman, L. S., Wcislo, P., Hill, C., Wilzewski, J. S.: HITRAN Application Programming Interface (HAPI), A comprehensive approach to working with spectroscopic data, J. Quant. Spectrosc. Radiat. Transfer 177, 15-30, 2016.

Korb, C. L. and Weng, C. Y.: Differential absorption lidar technique for measurement of the atmospheric pressure profile, Appl. Opt., 22, 3759-3770, 1983.

Lawrence, R., Lin, B., Harrah, S., Hu, Y., Hunt, P., and Lipp, C.: Initial flight test results of differential absorption barometric radar for remote sensing of sea surface air pressure, Journal of Quantitative Spectroscopy & Radiative Transfer, 112, 247-253, 2011.

Lin, B, Ismail, S., Harrison, F. W., Browell, E. V., Nehrir, A. R., Dobler, J., Moore, B., Refaat, T., and Kooi, S. A.: Modeling of intensity-modulated continuous-wave laser absorption spectrometer systems for atmospheric CO2 column measurements, Applied Optics, 52, 7062-7077, 2013.

Lin, B., and Hu Y.: Numerical simulations of radar surface air pressure measurements at O2 bands, Geoscience Remote Sens. Lett., 2, 324-328, 2005.

Lin, B., and Liu, Z.: Martian atmospheric CO2 and pressure profiling with differential absorption lidar: System consideration and simulation results. Earth and Space Science, 8, e2020EA001600. https://doi. org/10.1029/2020EA001600, 2021.

Lin, B., Nehrir, A., Harrison, F., Browell, E., Ismail, S., Obland, M., Campbell, J., Dobler, J., Meadows, B., Fan, T., and Kooi, S.: Atmospheric CO2 column measurements in cloudy conditions using intensity-modulated continuous-wave lidar at 1.57 micron, Optics Express, 23, A582 – A593. DOI:10.1364/OE.23.00A582, 2015.

Natraj, V., Luo, M., Blavier, J.-F., Payne1, V. H., Posselt, D. J., Sander, S. P., Zeng, Z., Neu, J. L., Tremblay, D., Wu, L., Roman, J. A., Wu, Y., and Dorsky, L. I.: Simulated multispectral temperature and atmospheric composition retrievals for the JPL GEO-IR Sounder. Atmos. Meas. Tech., 15, 1251–1267, https://doi.org/10.5194/amt-15-1251-2022, 2022.

Refaat, T., Singh, U., Yu, J., Petros, M., Ismail, S., Kavaya, M., and Davis, K.: Evaluation of an airborne triple-pulsed 2 µm IPDA lidar for simultaneous and independent atmospheric water vapor and carbon dioxide measurements, Appl. Opt., 54, 1387–1398, 2015.

Seiff, A., and Kirk, D.: Structure of the atmosphere of Mars in summer at mid-latitudes, J. Geophys. Res., 28, 4364-4378, 1977.

https://doi.org/10.5194/amt-2023-180
Preprint. Discussion started: 20 November 2023

Atmospheric Measurement Techniques
Discussions

Smith, D., Zuber, M., and coauthors: The Global Topography of Mars and Implications for Surface Evolution, Science, 284, 1495; DOI: 10.1126/science.284.5419.1495, 1999.

Spiga, A., Forget, F., Dolla, B., Vinatier, S., Melchiorri, R., Drossart, P., Gendrin, A., Bibring, J.-P., Langevin, Y., and Gondet, B.: Remote sensing of surface pressure on Mars with the Mars Express/OMEGA spectrometer: 2. Meteorological maps. J. Geophys. Res., 112, E08S16, doi:10.1029/2006JE002870, 2007.

Sun, X., Abshire, J. B., Beck, J. D., Mitra, P., Reiff, K., and Yang, G.: HgCdTe avalanche photodiode detectors for airborne and spaceborne lidar at infrared wavelengths. Optics Express, 26, 16589-16602, 2017.

Williams, D., Mars Fact Sheet, Last updated on 15 June 2020. (https://nssdc.gsfc.nasa.gov/planetary/factsheet/marsfact.html.)

Yu, J., Petros, M., Singh, U. N., Refaat, T. F., Reithmaier, K., Remus, R. G., and Johnson, W.: An Airborne 2-mm Double-Pulsed Direct-Detection Lidar Instrument for Atmospheric CO2 Column Measurements, Journal of Atmospheric And Oceanic Technology, 34, 385-400, 2017.

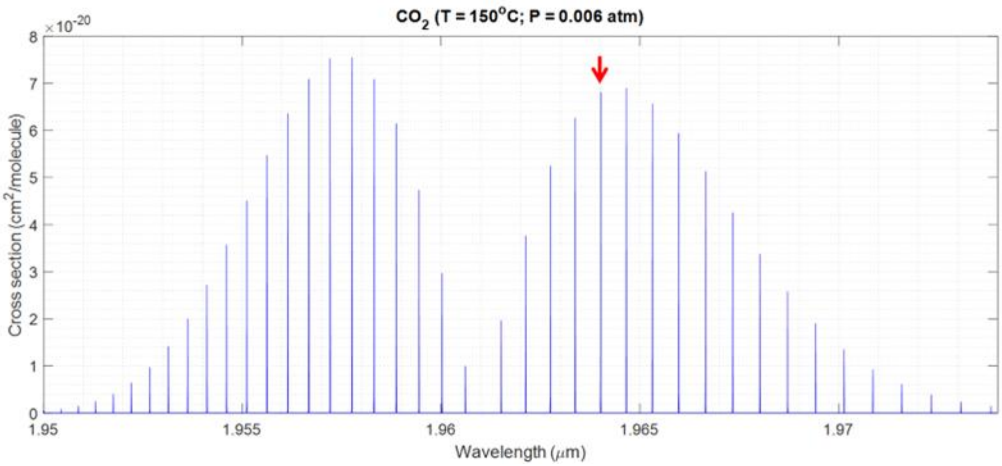

Figure 1: Line-by-line calculated CO_2 absorption spectrum of the ν′(20011) vibrational band for T = 150˚C and P = 0.006 atm using the HITRAN Application Programming Interface (HAPI) software. The red arrow indicates the absorption line selected (i.e., P(10)) in this paper.

https://doi.org/10.5194/amt-2023-180
Preprint. Discussion started: 20 November 2023

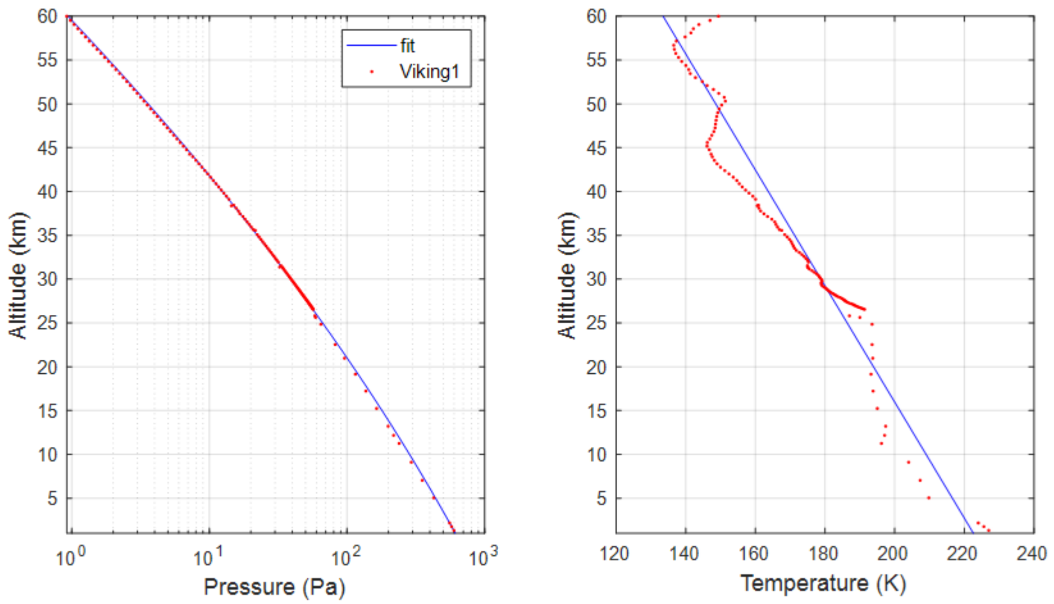

Figure 2: Pressure (left) and temperature (right) profiles on Mars measured by Viking 1 (red dots) and modeled (blue curves).

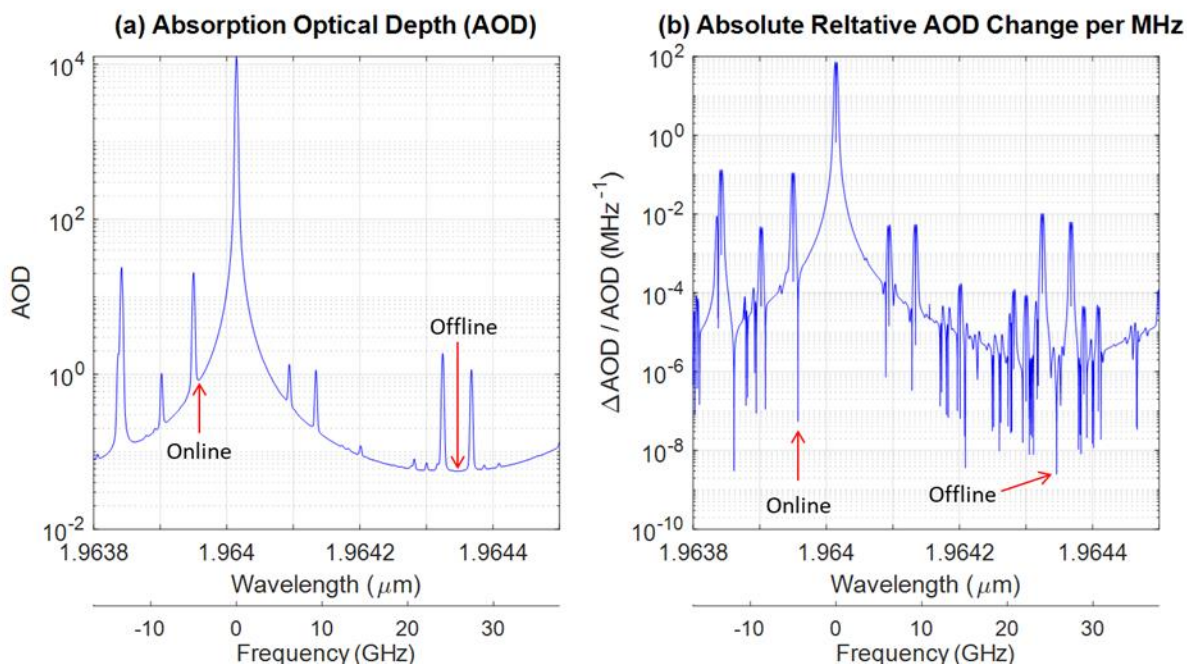

Figure 3: (a) CO_2 absorption optical depth (AOD) for Mars and (b) its absolute value of change for a 1 MHz variation in laser frequency. The arrows indicate the selected online and offline laser wavelengths.

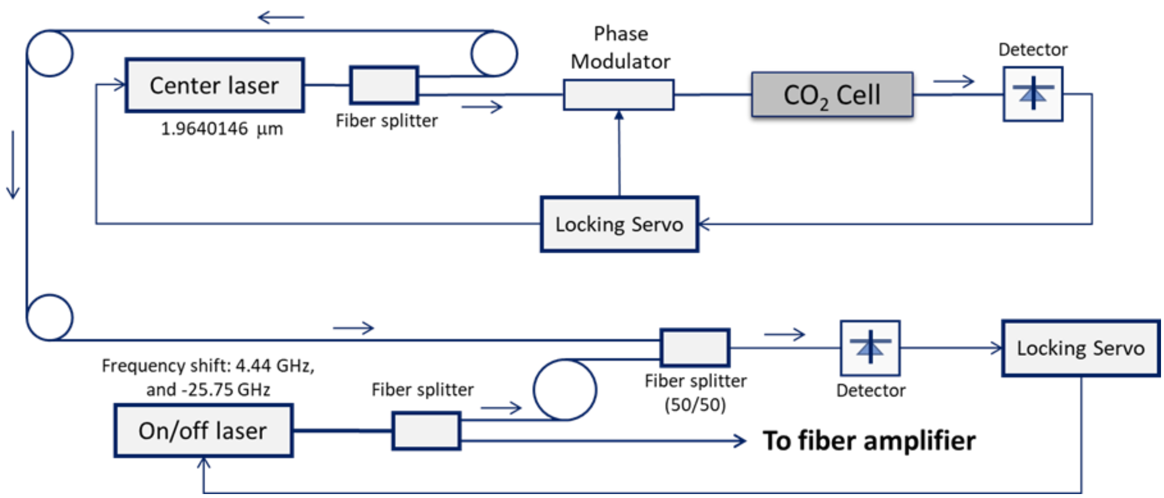

Figure 4: Conceptual diagram for master laser wavelength locking and control.

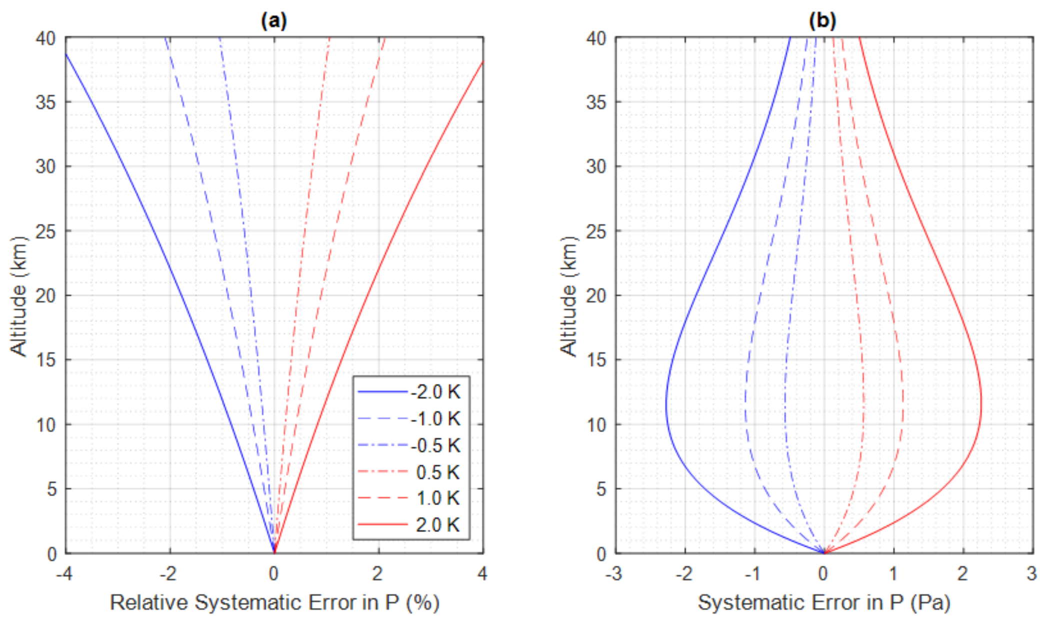

Figure 5: (a) Relative systematic error and (b) systematic error in pressure P as a function of altitudes due to a bias of 0.5 K, 1.0 K, and 2.0 K in temperature T, calculated using Eq. (12).

https://doi.org/10.5194/amt-2023-180
Preprint. Discussion started: 20 November 2023

Atmospheric Measurement Techniques Discussions

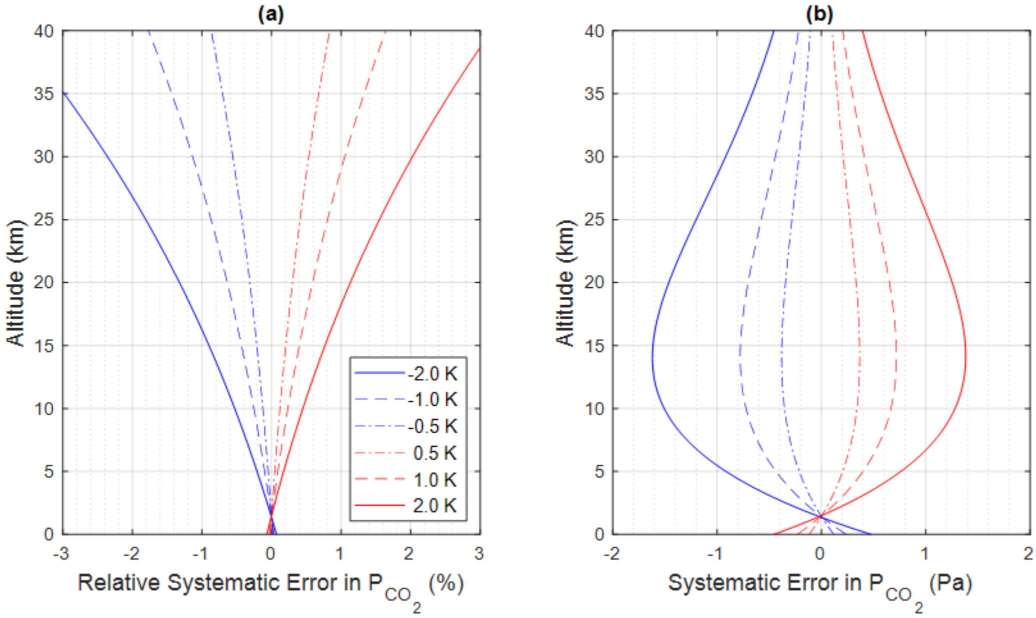

Figure 6: (a) Relative system error and (b) error in P_{CO2} retrieved from CO_2 DAOD due to ±0.5 K, ±1.0 K, and ±2.0 K bias in T, calculated using HAPI.

https://doi.org/10.5194/amt-2023-180
Preprint. Discussion started: 20 November 2023

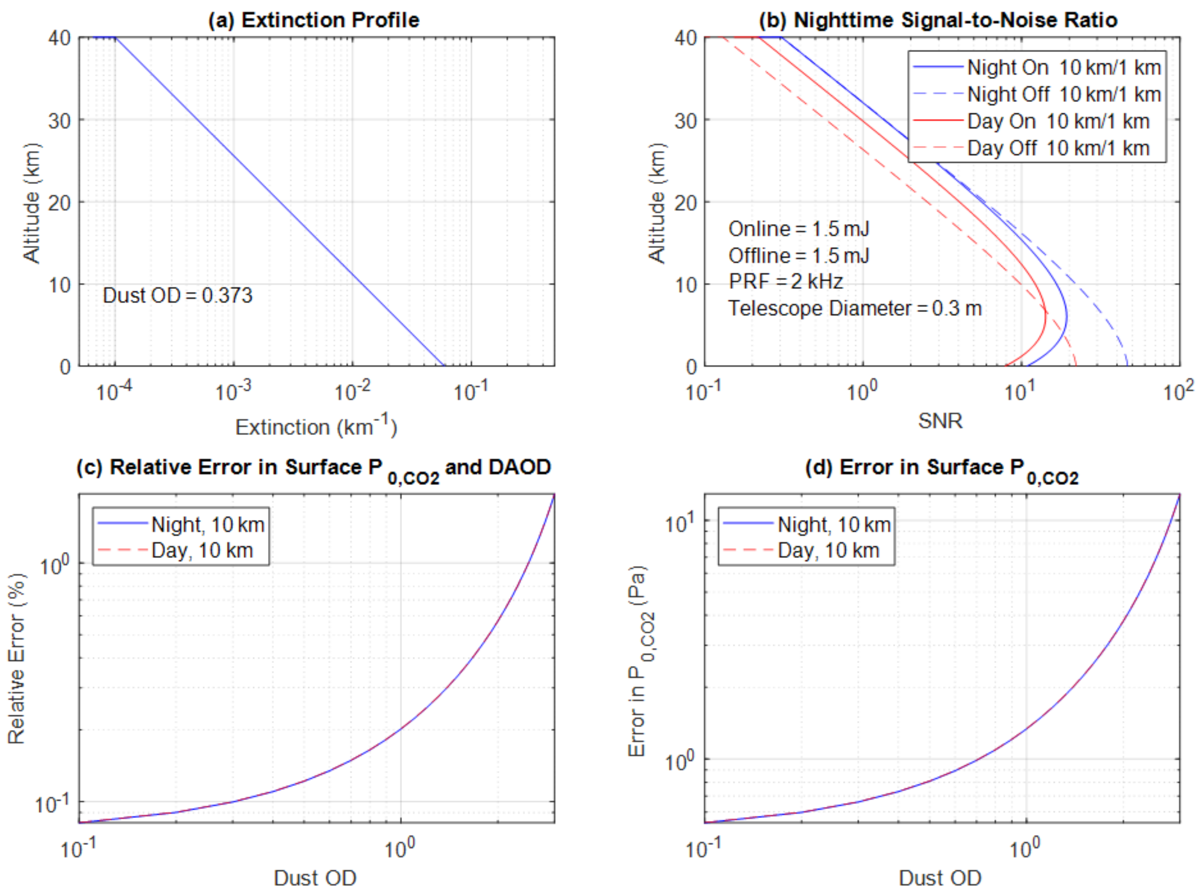

Figure 7: (a) Modelled dust extinction distribution, (b) SNRs for the online and offline wavelength at a horizontal resolution of 10 km and vertical resolution of 1 km during day and night, (c) relative errors in the CO_2 DAOD measurement and (d) errors in P_{CO2} due to random noise.

Table 1 Comparisons of space lidar measurements on Mars and Earth

		Mars 1.964 µm	CALIPSO/Earth 0.532 µm	Figure of Merit	Remark
Satellite	height (km)	250	710	8.05	signal ~ 1/height^2
	on ground speed (km/s)	3.45	7.5	2.17	signal ~ 1/speed
Photon number per mJ		10.320e+27	2.6782e+27	3.85	signal ~ N_{photon}
Solar radiation	constant (kW/m^2)	0.59	1.361	2.3	background noise ~ solar radiation
	visible to IR irradiance ratio			~ 220	
Atmospheric backscatter		Dust from surface up to ~50 km	Aerosol in the low atmosphere		signal ~ backscatter

https://doi.org/10.5194/amt-2023-180
Preprint. Discussion started: 20 November 2023

Atmospheric Measurement Techniques Discussions

425 **Table 2 Lidar system parameters used in OSSEs**

Laser	pulse energy, online / offline (mJ)	1.5 / 1.5
	pulse repetition frequency (Hz) of each wavelength	2000
	pulse width (ns)	200
	beam expander throughput	0.883
	Wavelengths: online, and offline (μm)	1.9639572, 1.9643460
Telescope	diameter (m)	0.3
	clear area ratio	0.882
Detector (DRS APD)	quantum efficiency	0.9
	fill factor	0.75
	dark current (A)	3.5e-13
	gain	900
Lidar receiver FOV (mrad)		0.13
Solar blocking filter bandwidth (nm)		0.8
System optical throughput		0.545
Sun zenith angle at equator (for daytime simulation)		30°
Surface reflectivity (sr^{-1})		0.161
Satellite altitude (km)		240